

Reconstructing the radial velocity profile of cosmic voids with kinematic Sunyaev-Zeldovich Effect

Yi-Chao Li^{1,2}, Yin-Zhe Ma^{2,3,*} and Seshadri Nadathur⁴

¹*Centre for Radio Cosmology (CRC), Department of Physics and Astronomy,*

University of the Western Cape, Modderdam Road, Bellville, Cape Town 7530, South Africa

²*School of Chemistry and Physics, University of KwaZulu-Natal,*

Westville Campus, Private Bag X54001, Durban 4000, South Africa

³*NAOC-UKZN Computational Astrophysics Centre (NUCAC),*

University of KwaZulu-Natal, Durban, 4000, South Africa and

⁴*Institute of Cosmology and Gravitation, University of Portsmouth, Burnaby Road, Portsmouth, PO1 3FX, UK*

We develop an estimator to extract the mean radial velocity profile of cosmic voids via the kinematic Sunyaev-Zeldovich effect of pairs of galaxies surrounding them. The estimator is tested with simulated pure kSZ map and void catalogue data from the same simulation. The results show that the recovered signal could be attenuated by low angular resolution of the map or large aperture photometry filter radius size, but the mean radial velocity profile can be fully recovered with our estimator. By applying the estimator to the *Planck* 2D-ILC CMB map, with galaxy and void catalogues from BOSS DR12, we find that the estimated void velocity profile is 3.31σ apart from null detection for voids with continuously rising density profiles asymptoting to the mean density; and 1.75σ for voids with positive density contrast shell surrounded. By fitting the reconstructed data to the theoretical profile, we find the reduced χ^2 to be 1.19 and 0.62 for the two types of void, respectively, indicating a good fit of the model to the data. We then forecast the detectability of the radial velocity profile of cosmic voids with future CMB surveys, including SPT-3G, AdvACT, and Simons Observatory. We find that the contamination effect from CMB residuals is negligible with survey area over 2,000 deg², especially with aperture photometry size less than 1 arcmin. But the effect from instrumental noise is non-negligible. For future SPT-3G, AdvACT and Simons Observatory, the detection is potentially achievable from 3σ to 10σ C.L., depending on specific instrumental parameters. This opens a new window of probing dynamics of the cosmic structures from the kinematic Sunyaev-Zeldovich effect.

I. INTRODUCTION

The kinematic Sunyaev-Zeldovich effect (hereafter, kSZ effect) is the secondary CMB anisotropy effect due to its scattering off moving electrons in the Universe [1, 2]

$$\frac{\Delta T}{T} = -\frac{\sigma_T}{c} \int dl n_e (\mathbf{v} \cdot \hat{\mathbf{n}}), \quad (1)$$

in which, σ_T is the Thomson cross-section, n_e is the electron density and \mathbf{v} is the peculiar velocity of electrons relative to the CMB. The kSZ signal was first detected by Ref. [3] via pairwise kSZ estimator proposed in Refs. [4, 5], using the CMB data from Atacama Cosmology Telescope (ACT [6]) and the galaxy catalogue from the Sloan Digital Sky Survey III DR9 [7]. Since then, there has been a number of works to detect the kSZ effect at various levels by cross-correlating CMB data with other large-scale structure tracers. These include the pairwise kSZ estimates with South Pole Telescope (SPT) data and Dark Energy Survey (DES) cross-correlation [8], Atacama Cosmology Telescope (ACT) data and SDSS/DR11 cross-correlation [9], *Planck* and SDSS/DR12 cross-correlation [10, 11]; kSZ cross-correlation with reconstructed peculiar velocity field [12, 13]; the squared kSZ field cross-correlation with projected density field from WISE infra-red survey [14, 15]; the kSZ dispersion measurement with *Planck* data and X-rays selected clusters [16]. More recently, Ref. [17] detected the rotational kSZ effect

with *Planck* map and six rotational cluster samples from SDSS/DR10.

Despite the rapid progress of kSZ detection in this field, little work has been done to investigate the behaviour of cosmic void, which is believed to dominate the cosmic volume on large scales. The cosmic voids refers to the large under-density region of matter distribution in the Universe. During the cosmic evolution, matters are accredited into the galaxies and clusters due to the gravitational attraction, therefore leaving more and more empty and underdense region in the Universe. The properties of the voids, such as the abundance or the spatial distribution, are related to the initial conditions and the universe evolution history [18, 19]. In the meanwhile, the voids properties also depend on the nature of the gravity [20, 21]. With N -body simulations, one can explore the gravitational physics of the void formation [22, 23], the statistical properties of the void distribution [19, 24], and the density and velocity profiles [25–28].

Recently, several cosmic void catalogues have been compiled from galaxy redshift survey data [29–32]. Studies with such cosmic void catalogue and numerical simulations suggest that it is possible to classify voids into two different types according to their surrounding density profiles. The “S-type” voids are surrounded by a shell of positive density contrast δ which compensates the mass deficit within the void. The “R-type” voids instead have continuously rising density profiles asymptoting to the mean density [33]. The different gravitational lensing effects on the CMB of these types of voids were recently detected [34]. The different density environment leads to different velocity fields around cosmic voids. Using mock galaxy and voids catalogue, Ceccarelli et al. [33] showed that S-type voids have infall velocities outside of the

*Electronic address: Ma@ukzn.ac.za

overdense shell whereas inside the overdense shell the voids are expanding. In contrast, R-type voids only expand and experience no contraction around void radius. Void velocity and density profiles can be measured observationally via the RSD effect in the void-galaxy cross-correlation [35–38] or through gravitational lensing by voids [34, 39].

In this paper, we investigate the radial velocity profile from the measurement of kSZ effect, and present the current measurement from *Planck* data and forecasts for future experiments. Our approach aims to provide a complementary method to understand the dynamical behaviour of cosmic voids than previous studies from N -body simulations, weak lensing and RSD effect. In Sec. II, we present the different types of the voids in the large-scale structure, and the estimator to extract the radial velocity profile of voids from kSZ effect. In Sec. III, we calculate the expected radial velocity profile from numerical simulations. In Sec. IV, we present the current measurement of the radial velocity profile from *Planck* maps and BOSS DR12 void catalogues. In Sec. V, the forecasts for future CMB experiments are presented and discussed, including ACT, SPT and Simons Observatory. The conclusion is presented in the last section.

Throughout this paper, we adopt a spatially flat Λ -Cold-Dark-Matter (Λ CDM) cosmology model with cosmological parameters fixed at *Planck* 2015 best-fitting values, i.e. $\Omega_b h^2 = 0.02230$, $\Omega_c h^2 = 0.1188$, $\Omega_k h^2 = 0.00037$ and $H_0 = 67.74 \text{ km s}^{-1} \text{ Mpc}^{-1}$ [40].

II. THE COSMIC VOIDS

A. Two types of cosmic voids

It is useful to characterise the population of voids into R-type and S-type [18, 26, 27, 37, 41]. The S-type voids usually lie within some overdense region of large-scale structure, therefore it is usually called “Void-in-cloud” scenario. In comparison, R-type of voids is usually embedded in the low-density region of large-scale structure, and therefore named as “Void-in-void”.

Ref. [42] investigated the gravitation potential environments of the voids and suggested a empirical linear relation between the averaged value of potential and the void properties,

$$\bar{\Phi}_0 = -a\lambda_v + c, \quad (2)$$

in which, a and c are positive constants determined from the simulation and the parameter λ_v is defined as

$$\lambda_v = \bar{\delta}_g \left(\frac{R_{\text{eff}}}{h^{-1} \text{Mpc}} \right)^{1.2} \quad (3)$$

where R_{eff} is the effective void size and $\bar{\delta}_g$ is the average galaxy density contrast over the void. The linear scaling of $\bar{\Phi}_0$ and λ_v is universal and relatively independent of the galaxy tracer properties. According to the analysis in [42], voids with larger values of λ_v , particularly $\lambda_v > 10$ for LOWZ/CMSS catalogue, are more strongly correlated with the regions of negative gravitational potential, $\Phi < 0$, and more likely to be

the S-type voids lying in the overdensity regions. In contrast, the smaller values of λ_v indicate the R-type voids with underdensity environments. In our analysis, we split the void catalogue in to two sub-samples with λ_v greater and less than 10. The R-type of voids is likely to have a positive velocity profile pointing outward from the center of the void; while the S-type of voids is likely to have a slightly negative velocity profile at the boundary region of the voids due to the overdense “wall” surrounding them. Recently, Raghunathan et al. [34] observationally confirmed the difference in void profiles with λ_v based on their CMB lensing signal.

B. The estimator of void radial velocity profile

1. The pairwise kSZ estimator

We want to use the relative velocity between the galaxies around a cosmic void to extract the radial velocity profile of the void. For this reason, we need to calculate the normal pairwise momentum estimator between two galaxies due to the normal gravitational attraction, then subtract this term from the true pairwise kSZ effect. The pairwise momentum estimator was initially proposed by Refs. [4, 5] and used in Hand et al. (2012) [3] to make the first detection of the kSZ effect. The estimator has been widely used in previous kSZ studies [8–12]. By selecting a pair of galaxies, i and j , we can measure the difference between CMB temperature fluctuations $\Delta_{ij} = T_i - T_j$. T_i and T_j are the CMB temperatures where the two galaxies locate, filtered with an aperture photometry (AP) filter or matched filter to removed the large-scale primary CMB contribution. The χ^2 function can be constructed as

$$\chi^2 = \sum_{i < j} [\Delta_{ij} - \Delta^{\text{P}}(r_{ij})P_{ij}]^2, \quad (4)$$

where indices i and j sum over all pairs without repetition. P_{ij} is the geometric operator that projects the pairwise velocity to the line-of-sight(LoS) direction. It can be expressed as [4, 5]

$$\begin{aligned} P_{ij} &= (\hat{\mathbf{r}}_{ij}) \cdot \frac{(\hat{\mathbf{r}}_i + \hat{\mathbf{r}}_j)}{2} \\ &= \frac{(r_i - r_j)(1 + \cos \theta)}{2\sqrt{r_i^2 + r_j^2 - 2r_i r_j \cos \theta}} \end{aligned} \quad (5)$$

where $\hat{\mathbf{r}}_{i,j} = \mathbf{r}_{i,j}/r_{i,j}$, $\hat{\mathbf{r}}_{ij} = (\mathbf{r}_i - \mathbf{r}_j)/r_{ij}$. r_i and r_j are the comoving distance of the galaxies i and j , respectively; and $r_{ij} = |\mathbf{r}_i - \mathbf{r}_j|$.

$\Delta^{\text{P}}(r)$ is the pairwise kSZ effect due to the mean pairwise velocities of the galaxies and it can be expressed with the mean CMB temperature T_{CMB} , the mean optical depth of the galaxies $\bar{\tau}$, speed of light c and the mean pairwise velocity $v^{\text{P}}(r)$ as,

$$\Delta^{\text{P}}(r) = -\frac{T_{\text{CMB}}\bar{\tau}}{c}v^{\text{P}}(r) \quad (6)$$

where r is the comoving separation distances between the pair of samples.

By minimizing the χ^2 function, $\partial\chi^2/\partial\hat{\Delta}^p = 0$ leads to the expression of estimator [3–5]

$$\hat{\Delta}^p(r) = \frac{\sum_{i<j} \Delta_{ij} P_{ij}}{\sum_{i<j} P_{ij}^2}. \quad (7)$$

We will apply the above estimator to *Planck* maps and simulated kSZ maps of, SPT-3G, ACT and Simons Observatory.

2. kSZ effect due to the void expansion

If the galaxies are near the void, they are pushed by the void in the direction away from its center. Therefore there is an outflow component to the velocity, $v^e(R)$, caused by the expansion of the void, where R is the radial distance relative to the void centre. We assume that each void share the same radial velocity profile normalised by the effective radius of the void, i.e. $v^e(R/R_{\text{eff}})$. We want to reconstruct this radial velocity profile by building an estimator $\hat{v}^e(R)$ for the observed kSZ map.

In the comoving frame, we define the vector from observer pointing to the center of the void as \mathbf{r}_o , and to the selected galaxy as \mathbf{r}_i . Then the vector from the void center to the galaxy sample is \mathbf{r}_{io} . Then projection of \mathbf{r}_{io} onto the LoS direction is

$$q_i = \hat{\mathbf{r}}_{io} \cdot \hat{\mathbf{r}}_i = \frac{r_i - r_o \cos \theta_{io}}{\sqrt{r_i^2 + r_o^2 - 2r_i r_o \cos \theta_{io}}}, \quad (8)$$

in which θ_{io} is the separation angle between the galaxy and the void centre. Then the velocity difference projected onto the LoS direction becomes $v^e(R)Q_{ij}$, where $Q_{ij} = q_i - q_j$. Then temperature difference due to the kSZ effect can be expressed as

$$\Delta_R^e Q_{ij} = -\frac{T_{\text{CMB}} \bar{\tau}}{c} v^e(R) Q_{ij}. \quad (9)$$

The χ^2 function can be expressed as

$$\chi^2 = \sum_{i<j} [\Delta_{ij} - (\Delta^p(r_{ij})P_{ij} + \Delta_R^e Q_{ij})]^2. \quad (10)$$

Taking the minimal condition as $\partial\chi^2/\partial\Delta_R^e = 0$, we obtain the estimator

$$\hat{\Delta}_R^e = \frac{\sum_{i<j} \Delta_{ij} Q_{ij}}{\sum_{i<j} Q_{ij}^2} - b_R, \quad (11)$$

where

$$b_R = \frac{\sum_{i<j} \Delta^p(r_{ij}) P_{ij} Q_{ij}}{\sum_{i<j} Q_{ij}^2} \quad (12)$$

is a bias term due to the normal gravitational attraction between galaxy pairs. Finally, the radial velocity profile of the void can be estimated as

$$\hat{v}^e(R) = -\frac{c}{T_{\text{CMB}} \bar{\tau}} \hat{\Delta}_R^e. \quad (13)$$

III. EXPECTED SIGNAL

A. Simulation data

We use one redshift snapshot at $z = 0.52$ from the Big Multi-Dark (BigMD) N -body simulation [43, 44], which follows the evolution of 3840^3 particles in a box of side $L = 2500 h^{-1} \text{Mpc}$ using GADGET-2[45] and adaptive refinement tree [46, 47] codes. The halo catalogues are formed by using the Bound Density Maximum algorithm [48, 49] and the underlying dark matter density field is determined from the full resolution simulation output on a 2350^3 grid using the cloud-in-cell interpolation.

- The *mock galaxy catalogues* are created by assigning galaxies to DM halo following a distribution based on the halo mass. The halos are populated according to the halo occupation distribution (HOD) model [50]. The catalogue contains central and satellite galaxies. In our analysis, we only use the central galaxies, which are good tracers of the clusters velocities. The central galaxies were placed at the center of their respective halos and the numbers of central galaxies in each mass bin follow a nearest integer distribution with the mean occupation function,

$$\langle N_{\text{cen}}(M) \rangle = \frac{1}{2} \left[1 + \text{erf} \left(\frac{\log M - \log M_{\text{min}}}{\sigma_{\log M}} \right) \right], \quad (14)$$

in which, the parameters M_{min} , $\sigma_{\log M}$ were chosen in order to match those the properties of the SDSS CMASS catalogue. For the details of mock galaxy catalogue generation, please refer to Nadathur et al. (2017)[42].

- The *voids catalogues* are identified using the REVOLVER void-finding algorithm [38], which is based on the earlier ZOBOV (ZOnes Bordering On Voidness) watershed void-finding algorithm [51]. REVOLVER estimates the local galaxy density field from the discrete galaxy distribution using a Voronoi tessellation method, which includes additional corrections for the survey selection function and angular completeness, described in detail in [31, 52]. The local minima in this field are identified as the center of the voids and the watershed basins around them are the void edges. Following the procedure of Ref. [52], the voids are identified with each individual density basin without any additional merging. The size of the void is characterized by the effective void radius $R_{\text{eff}} = (3V/4\pi)^{1/3}$, where V is the total void volume determined from the sum of its Voronoi cells volume.

B. Simulated kSZ signal

We use the position and velocity information of the central galaxies to simulate the kSZ signal. The mock galaxy catalogue is firstly split into 5 sub-catalogues along the $\hat{\mathbf{z}}$ -axis, which is chosen as the Line-of-Sight (LoS) direction. Each of the sub-catalogues is assigned new radial comoving distance

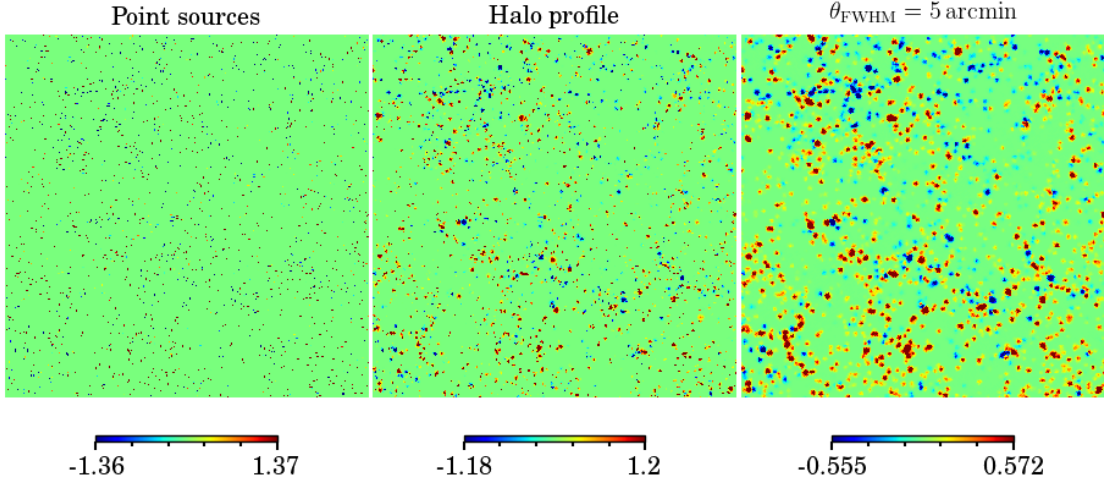


FIG. 1: Simulated kSZ maps. *Left*—assuming point sources; *Middle*—assuming Gaussian halo profile for the clusters; *Right*: Gaussian halo profile map smoothed with Gaussian beam function with $\theta_{\text{FWHM}} = 5$ arcmin. The color ranges for all the plots are in unit of μK and truncated at $\pm 3\sigma$.

with median values equal to the comoving distance at redshift $z = 0.52$.

The kSZ temperature anisotropies is given by

$$\Delta T_{\text{kSZ}} = -\frac{T_{\text{CMB}}\bar{\tau}}{c}v_{\text{LoS}} \quad (15)$$

in which, $\bar{\tau}$ is a free rescaling parameter as an average optical depth of the central galaxy samples. We assume $\bar{\tau} = 10^{-3}$ for the simulation. We will show later, that this parameter is sensitive to the choice of samples, angular resolution of the CMB map and the filter size of aperture photometry (AP). v_{LoS} denotes the LoS component of peculiar velocity of free electrons.

At the stage-1 of simulation, we assume the clusters to be point sources and traced by the central galaxies. We project the central galaxy catalogues to the HEALPix maps with $N_{\text{side}} = 2048$. The pixels with galaxies are assigned the kSZ temperature according to Eq. (15). A $10^\circ \times 10^\circ$ patch of the simulated map is shown in the left panel of Fig. 1.

At the stage-2 of the simulation, we include the halo profile for the clusters. The velocity within the clusters is assumed to be constant and the $\bar{\tau}$ follows halo profile. To simplify the analysis, we use Gaussian halo profile.

$$\tau(r) = \bar{\tau} \exp\left[-\frac{r^2}{\sigma_{\text{vir}}^2}\right], \quad (16)$$

in which, r is the angular separation of the LoS to the halo center; and σ_{vir} is the angular size of the halo virial radius. The halo virial radius is estimated according to the halo virial

mass individually [53],

$$M_{\text{vir}} = \frac{4\pi}{3} [\Delta_c(z)\rho_c(z)]r_{\text{vir}}^3$$

$$\Delta_c(z) = 18\pi^2 + 82[\Omega(z) - 1] - 39[\Omega(z) - 1]^2, \quad (17)$$

where $\rho_c(z) = \rho_{c0}E^2(z)$ is the critical density at redshift z . $\rho_{c0} = 1.879 h^2 \times 10^{-29} \text{ g cm}^{-3}$, $E(z) = \sqrt{\Omega_m(1+z)^3 + \Omega_\Lambda}$, and $\Omega(z) = \Omega_m(1+z)^3/E^2(z)$. The middle panel of Fig. 1 shows the simulated map with halo profile applied.

At the stage-3 of the simulation, we convolve the simulated maps with Gaussian beam of $\theta_{\text{FWHM}} = 5$ arcmin. The smoothed patch is shown in the right panel of Fig. 1.

C. Radial velocity profile

We first calculate the radial velocity profile of cosmic voids as black step lines in Fig. 2. Since each void has different radius, we plot the radial velocity profile as a function of normalized radius R/R_{eff} , where R_{eff} is the effective void radius. The void catalogue is split into R-type and S-type subsamples according to the void parameter λ_v . The left panel of Fig. 2 shows the case with R-type voids ($\lambda_v < 10$) and right panel shows the S-type voids ($\lambda_v > 10$). One can see that, a significantly different radial velocity profiles between these two types are shown. The R-type voids have a positive velocity profile up to the radial distance of 5 times of void effective radius, indicating an overall expansion of the voids. The velocity profile of the S-type voids is positive within the void effective radius and negative outside, which indicates that at the boundary region the structures are actually collapsing. This velocity structure is

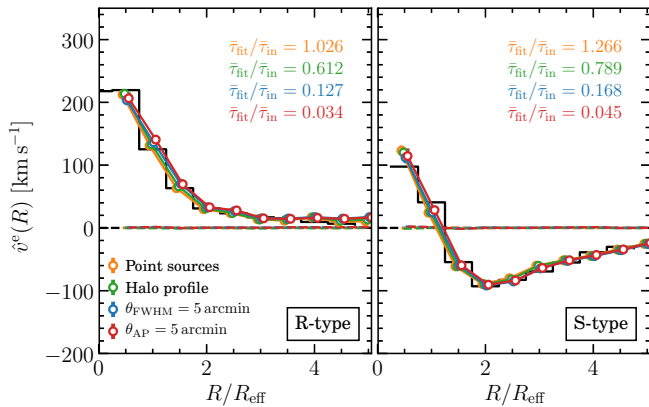


FIG. 2: *Left*—the results for voids with $\lambda_v < 10$ (R-type); *Right*—the results for voids with $\lambda_v > 10$ (S-type). The black step line shows the theoretical radial velocity profile which is directly read from the simulated catalogue. The estimate radial velocity profiles with different stages of simulation maps are fit to the theoretical curve with $\bar{\tau}$ as the free fitting parameter. The ratio of the fitted $\bar{\tau}_{\text{fit}}$ to input $\bar{\tau}_{\text{in}}$ are also list, where $\bar{\tau}_{\text{in}} \equiv 10^{-3}$. The dashed lines are the mean \hat{v}^e estimated with the pixels randomly-shuffled CMB temperature values (see Sect. (IV B) for details).

consistent with the previous investigation of the radial density profile through numerical simulations [18, 27, 35].

We then test the behaviour of our estimator (Eqs. (11)-(13)) with simulated kSZ maps at the three different stages as mentioned in Sect. III B and Fig. 1. We first estimate the the voids expansion rate by using our estimator (Eq. (13)) and then fit the estimated \hat{v}^e to the theoretical prediction with $\bar{\tau}$ as the free scaling parameter. The values of $\bar{\tau}_{\text{fit}}/\bar{\tau}_{\text{in}}$, which are the ratio of best-fitting to the initial input value of $\bar{\tau}_{\text{in}} \equiv 10^{-3}$, are list in the legend with corresponding colors for each individual simulation stage.

The radial velocity profile estimated with the first stage simulation map, which assumes the cluster to be point sources, is shown with orange color. Both the results for R-type and S-type voids are fitted to the theoretical predictions very well. The values of $\bar{\tau}_{\text{fit}}/\bar{\tau}_{\text{in}} = 1.026 \pm 0.04$ for R-type of voids, which is consistent with unity. For S-type voids, $\bar{\tau}_{\text{fit}}/\bar{\tau}_{\text{in}} = 1.266 \pm 0.06$, which indicates a larger $\bar{\tau}$ comparing to the mean values. A possible reason is that, the S-type voids are mostly located in overdense region, where the $\bar{\tau}$ is over the global mean values.

The results with the simulation maps considering the halo profiles are shown as green lines; and the results with further including the beam smoothing effect are shown as blue lines. Both of these two sets of results are fitted to the theoretical predictions very well, except for the decreasing values of the $\bar{\tau}_{\text{fit}}/\bar{\tau}_{\text{in}}$. Therefore, both Gaussian profile and the beam effect can smooth the signal of the void expansion effect, producing a lower estimated value for the mean optical depth of clusters.

In the kSZ studies with real observational data, the primary fluctuation of the CMB is usually the contaminant factor at the background level. Therefore, the aperture photometry method

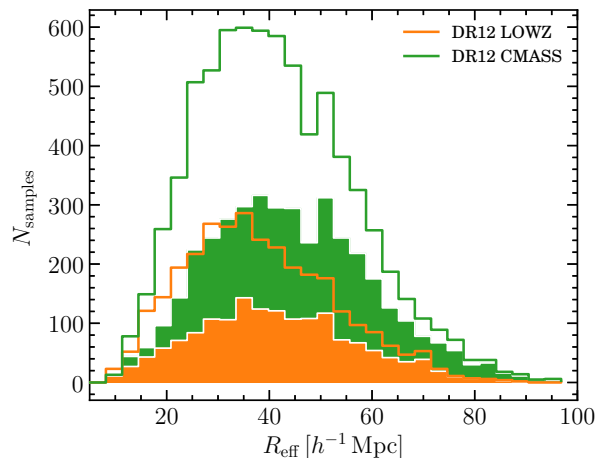


FIG. 3: The empty histograms show the distribution of the total LOWZ/CMASS (orange/green) void catalogue; The filled histograms show the distribution of the void with $\lambda_v < 10$ (R-type voids). The difference between empty and filled histograms is therefore for S-type voids, which have $\lambda_v > 10$.

(AP) is usually used as a filter to remove the long-wavelength mode fluctuations of the CMB [9, 11, 13]. In the AP method, we compute the average temperature within a given angular radius θ and subtract from it the average temperature in a surrounding ring with inner and outer radii $[\theta, \sqrt{2}\theta]$. This method is model-independent and blinds to any specific model of spatial distribution of gas. As suggested by Ref. [11], we use the aperture size $\theta_{\text{AP}} = 5$ arcmin which can optimize the detection.

We apply the AP filter to our Stage-3 simulation and show the results in red lines in Fig. 2. One can see that the profile can be well fitted by the theoretical velocity profile, but the mean optical depth is reduced by almost 2 orders of magnitude. The signal reducing due to the smoothing effect makes the detection harder if systematic noise, such as the equipment noise, CMB and thermal SZ residuals are presented.

IV. MEASUREMENTS WITH *PLANCK* MAPS

A. Data

Here we present the real data in our estimation of radial velocity profile of cosmic voids.

a. Planck CMB maps We use two different thermal SZ-free CMB maps in our study to cross-check the consistency. One is the 2D-ILC CMB map, which is obtained by applying the ‘Constrained ILC’ component separation method [54] to the public *Planck* 2015 data¹. This algorithm is similar to the *Planck* NILC method [55, 56] which performs a minimum-

¹ <http://pla.esac.esa.int/pla>

variance weighted linear combination of the 9 *Planck* frequency maps, with weights calculated to give response to CMB spectral distortion. In addition to this, the algorithm is designed to nullify the tSZ signal so there is no tSZ bias and variance in this map. The Full-Width-Half-Maximum (FWHM) of the map is $\theta_{\text{FWHM}} = 5$ arcmin. For more details of the 2D-ILC map, we refer to Refs. [54] and [16].

As a comparison, we also use the SMICA-noSZ map from *Planck* survey [57] in this analysis. The Spectral Matching Independent Component Analysis (SMICA) method produces a foreground-cleaned CMB map from a linear combination of multi-frequency sky maps in harmonic space [58]. Similar to 2D-ILC map, this method also imposes a linear constraint to nullify the frequency dependence of the tSZ. The angular resolution of the SMICA-noSZ map is the same as 2D-ILC map.

The major difference between the two methods is that the 2D-ILC map uses wavelet decomposition to clean foregrounds locally both in pixel space and harmonic space, whereas the *Planck* SMICA-noSZ map is performed only in harmonic space. In addition, the 2D-ILC map was produced based on *Planck* 2015 data release, while the SMICA-noSZ map is based on *Planck* 2018 data release. Therefore, SMICA-noSZ map is less noisy and also has some improvements on calibrations of *Planck* instrumental systematics.

b. Central Galaxy Catalogue We adopt the galaxy catalogue of the twelfth data release of the Baryon Oscillation Spectroscopic Survey (BOSS DR12) and further select the ‘‘Central Galaxies’’ from the catalogue. The BOSS sample is designed to measure the BAO signature in two-point correlation function of the galaxy clustering. The BOSS/DR12 catalogue is separated into ‘‘LOWZ’’ and ‘‘CMASS’’ catalogues. Both catalogues include two separated survey areas, located in Northern and Southern Galactic Caps (NGC and SGC). In our analysis, we combine NGC and SGC samples.

The ‘‘LOWZ’’ samples span the redshift below 0.45; and the ‘‘CMASS’’ samples span the redshift between 0.45 and 0.8 [59]. We cut off samples with $z < 0.01$. We further reduce the catalogue by choosing the ‘‘Central Galaxies’’ which are isolated and dominant galaxies with no other galaxies within 1.0 Mpc in the transverse direction and redshift difference smaller than $1,000 \text{ km s}^{-1}$ [11, 60]. The selected central galaxies samples are regarded as the good indicator of the gravity center and therefore represent the clusters’ center positions. We refer the reader to Ref. [11] for more details of the selection process.

c. Void catalogue The void catalogue used in our analysis are also generated with the BOSS DR12 LOWZ/CMASS LSS galaxy samples [52] and identified via REVOLVER void-finding algorithm, which is the same method as we used for our simulation void catalogue. The void size distribution of the LOWZ/CMASS void catalogue are shown in Fig. 3. The empty histograms in Fig. 3 show the void size distribution of the total void catalogue, with orange color for LOWZ catalogue and green color for CMASS catalogue, respectively. The size distribution of the R-type voids, which are void with $\lambda_v < 10$ is shown with the filled histogram and the differences between empty and filled histogram show the distribution of

S-type voids. One can see that for both R-type and S-type voids in both LOWZ and CMASS catalogues, the peak distribution of the void size is around $R_{\text{eff}} \approx 40 h^{-1} \text{ Mpc}$. The total number of R-type and S-type voids for LOWZ are 1,462 and 1,348 and for CMASS are 3,845 and 3,122, shown in Table I. This indicates that CMASS volume contains more voids than LOWZ volume, and within each survey volume there is similar number of R-type and S-type voids. There’s no significant difference in voids size distribution between R-type and S-type voids.

B. Results of computation

The results estimated with the *Planck* 2D-ILC CMB map and LOWZ/CMASS galaxy and void catalogue are shown in Fig. 4. The black step line is the same as in Fig. 2, which is the theoretical prediction of the void expansion rate from simulation.

The error of the measurements is estimated by randomly-shuffling N times the AP filtered CMB temperature values, which have galaxy samples located in. The AP filter is applied before shuffling pixels. With such mock samples, the voids relative position and involved galaxy number are kept the same, but the LSS correlation are broken due to the shuffling. The covariance matrix is then estimated as

$$C_{ij}^{\text{mock}} = \frac{1}{N-1} \sum_{k=1}^N \left(\hat{v}_k^e(R_i) - \langle \hat{v}^e(R_i) \rangle \right) \left(\hat{v}_k^e(R_j) - \langle \hat{v}^e(R_j) \rangle \right) \quad (18)$$

in which i and j are the indices of the R/R_{eff} bins, in which we have 10 radius bins in this study. $\hat{v}_k^e(R)$ is the estimated radial velocity with the k -th mock void catalogue realization; $\langle \hat{v}^e(R) \rangle$ is the mean of N realizations and shown with the dashed lines in Fig. 4. We use $N = 300$ in our analysis and confirm that the covariance estimation is converged for $N \geq 300$. The diagonal terms of the covariance matrix are used as the error of the measurements, shown in Figs. 4 and 2. The correlation coefficient matrix is then estimated via,

$$E_{ij} = \frac{C_{ij}^{\text{mock}}}{\sqrt{C_{ii}^{\text{mock}} C_{jj}^{\text{mock}}}}, \quad (19)$$

which is shown in Fig. 6. The correlation coefficient matrix for LOWZ and CMASS are shown in the left and right panels, respectively. In each panel, the results for R-type voids are shown in the upper triangle region; while the S-type voids are shown in the lower triangle region. As we can see, at the larger R/R_{eff} bins, the results are more correlated between bins. The correlation between bins is due to the sharing of galaxy samples between different voids. The galaxy samples located far from the void center have higher chance to be involved in different voids. Also we can see that the LOWZ samples are less correlated comparing to CMASS. It is because the CMASS samples are located at higher redshifts, and, given the similar voids size distribution between CMASS and LOWZ, galaxy samples at high redshift have more chance to be shared between voids.

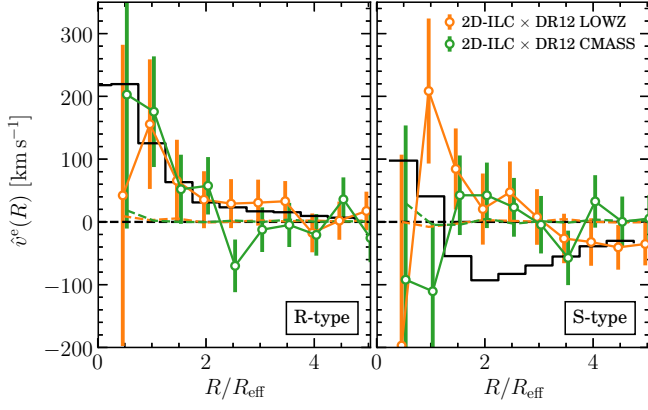


FIG. 4: The estimated $\hat{v}^e(R)$ with *Planck* 2D-ILC CMB map and LOWZ/CMASS (orange/green) void catalogue. The black step line shows the theoretical prediction which is directly read from the simulated catalogue. The *left* and *right* panels show the results for R-type and S-type voids, respectively. The estimated kSZ temperature difference are converted to velocity using Eq. (6). We use the $\bar{\tau}$ fitted with R-type results for both R-type and S-type temperature-velocity conversion. The fitted $\bar{\tau}$ values are summarized in Table I.

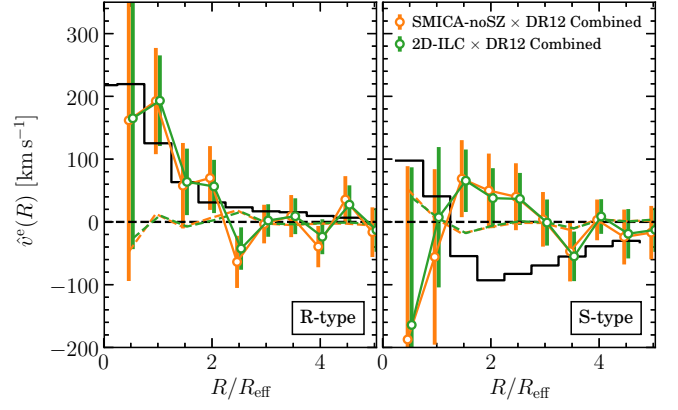


FIG. 5: Same as Fig. 4, but using *Planck* SMICA-noSZ/2D-ILC maps (orange/green) and combined LOWZ and CMASS catalogue. We use the $\bar{\tau}$ fitted with R-type results for both R-type and S-type temperature-velocity conversion. The fitted $\bar{\tau}$ values are summarized in Table I.

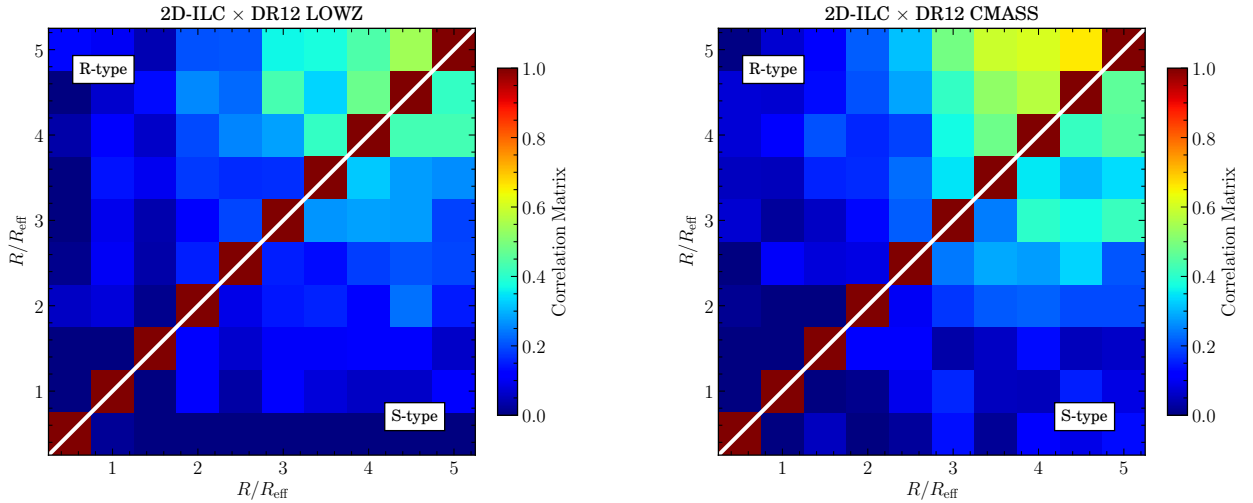


FIG. 6: The correlation coefficient matrix for the measurements of *Planck* 2D-ILC map with DR12 LOWZ/CMASS void catalogue (top-left/right panels, respectively); and *Planck* SMICA-noSZ/2D-ILC map with combined DR12 LOWZ and CMASS void catalogue (bottom-left/right panels, respectively). In each panel, the upper triangle shows the correlation coefficient matrix of the R-type voids; and lower triangle shows the S-type.

The results for R-type voids ($\lambda_v < 10$) are shown in the left panel. The estimated kSZ temperature difference are converted to velocity by using Eq. (6). The radial velocity profile for R-type voids is consistent with the theoretical predictions within the errors. The fitted $\bar{\tau} = (1.24 \pm 0.79) \times 10^{-4}$ and $(0.87 \pm 0.46) \times 10^{-4}$ for LOWZ and CMASS, respectively, which are consistent with the results measured with pairwise kSZ of clusters [11] within the error.

To quantify the level of detection, we define χ_{NULL}^2 and

χ_{reduced}^2 as follows

$$\chi_{\text{NULL}}^2 = \sum_{ij} \hat{v}^e(R_i) (C^{-1})_{ij} \hat{v}^e(R_j), \quad (20)$$

$$\chi_{\text{reduced}}^2 = \chi_{\text{min}}^2 / \text{d.o.f.} \quad (21)$$

where, d.o.f. = $N_{\text{bins}} - N_{\text{parameters}}$, and

$$\chi_{\min}^2 = \min \left[\sum_{ij} \left(\hat{v}^e(R_i) - v^t(R_i) \right) \left(C^{-1} \right)_{ij} \left(\hat{v}^e(R_j) - v^t(R_j) \right) \right]. \quad (22)$$

The C^{-1} is the inverse of the covariance matrix. Besides the covariance matrix estimated with the mock void samples, we further include the covariance of the intrinsic error C^{intr} , which is due to the intrinsic scattering of the velocity within the R/R_{eff} bins. The intrinsic covariance is estimated via velocities read directly from the simulation and it contributes $\lesssim 1\%$ of the uncertainties to the total variance. But when the variance is reduced by using more samples, the intrinsic variance contributes is up to $\lesssim 10\%$. Finally, we apply the Hartlap factor [61] to correct the biased inverse covariance matrix. The C^{-1} is finally defined as

$$C^{-1} = \frac{N - N_{\text{bin}} - 2}{N - 1} \left(C^{\text{mock}} + C^{\text{intr}} \right)^{-1}. \quad (23)$$

Equation (20) quantifies the detection of the signal with respect to null, where indices i and j run over all radius bins; and Eq. (21) quantifies the goodness of fit. We summarize our quantification in Table I.

1. Null detection

In Figs. 4 and 5, we plot the reconstructed peculiar velocities $\hat{v}^e(R)$ with *Planck* 2D-ILC and SMICA-noSZ maps and LOWZ/CMASS void catalogues. We list the detailed values of null detection for each respective case in Table I. One can see that, for LOWZ catalogue, detection of R-type void is similar to the case of S-type void, and the χ_{NULL}^2 values are in the range of 7.11 to 8.78 depending on which CMB maps are used. One can further convert the χ_{NULL}^2 value into the “ p -value”, which is defined as the probability of no detection given the measurement, i.e.

$$p = \text{Erfc} \left(\sqrt{\frac{\chi_{\text{NULL}}^2}{2}} \right), \quad (24)$$

where “Erfc” is the complementary error function. Therefore, for LOWZ catalogue, the probability of null detection of R-type and S-type voids for using two different versions of *Planck* CMB map is at 5×10^{-3} level, indicating $\sim 3\sigma$ C.L. detection of the two types of voids.

For CMASS catalogue, the R-type void is better detected than the S-type void, due to its uniformly expanding structure. The detection of R-type void is boosted to $\chi_{\text{NULL}}^2 = 17.79$ for 2D-ILC map and 14.69 for SMICA-noSZ map. This corresponds to the p -value as 2.47×10^{-5} for 2D-ILC map and 1.27×10^{-4} for SMICA-noSZ map. For S-type void, the χ_{NULL}^2 is around 6.5, which corresponds to $p = 1.04 \times 10^{-2}$.

In Table I, we also list the χ_{NULL}^2 for the combined LOWZ and CMASS catalogues. For R-type void, by using 2D-ILC map it reaches 21.86, and by using SMICA-noSZ map, it

reaches 21.32. These correspond to the p -values in the range of $(2.93 - 3.89) \times 10^{-6}$. The S-type void detection is reduced to $\chi_{\text{NULL}}^2 \simeq 6.1$ for the 2D-ILC map, for which p -value is 1.35×10^{-2} .

To summarize, the probability of null detection for R-type and S-type voids are 2.93×10^{-6} and 1.35×10^{-2} for the *Planck* 2D-ILC map, so the R-type and S-type voids are detected at 3.31σ and 1.75σ C.L. respectively.

2. Measuring expansion profile

For R-type voids, *Planck* 2D-ILC map gives $\chi_{\text{reduced}}^2 = (0.33, 1.34, 1.19)$ with the DR12-LOWZ, DR12-CMASS and the combination of such two voids catalogue, respectively. The lower χ_{reduced}^2 indicates that the results is over-fitted. It might be because the signal is attenuated due to the smear effect of the large AP filter. We have 1.54σ (weak) detection of the $\bar{\tau}$ with LOWZ catalogue, 1.94σ with CMASS catalogue and 2.68σ with the combination of such two catalogues.

For S-type voids, the reconstructed velocity profile is biased and the fitted $\bar{\tau}$ is consistent with 0. This large uncertainty of estimates is due to the instrumental noise, CMB residual and other residual foreground. The estimated results are shown in right panel of Fig. 4. The estimated kSZ temperature difference is also converted to velocity using Eq. (6). However, we use the fitted $\bar{\tau}$ with R-type voids, instead of the S-type voids. We also did the estimation by replacing the 2D-ILC map with SMICA-noSZ map and find very similar results to Fig. 4. We then combine the DR12 LOWZ and CMASS samples and stack the radial velocity profile against the 2D-ILC and SMICA-noSZ maps, and show in Fig. 5. One can see that the error-bars for both cases shrink and there is a clear detected signal for R-type of voids. For S-type of voids, there is still a large bias existed, due to its “cross-zero line” structure.

We then measure the value of optical depth ($\bar{\tau}$) by fitting the theoretical void expansion profile (black step line) to the data, and show our results in Table I. The $\bar{\tau}$ value is measured to be $(1.03 \pm 0.38) \times 10^{-4}$ for the R-type void, and $(-0.17 \pm 0.24) \times 10^{-4}$ for the S-type void.

V. FORECAST FOR FUTURE CMB EXPERIMENTS

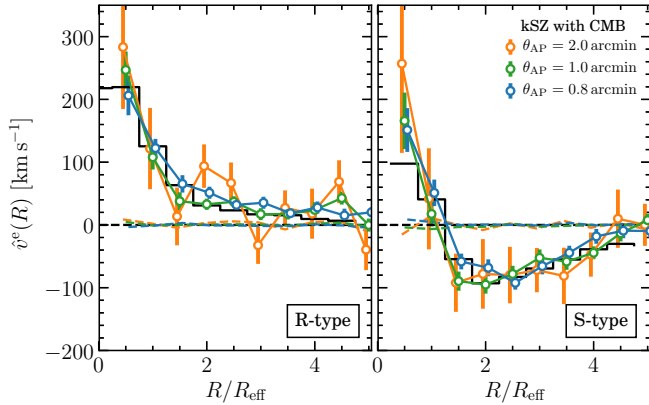
A. CMB residuals

The major contaminations to the signal come from the CMB temperature fluctuations, which are supposed to be filtered out with the designed filter. However, the residual of the CMB temperature fluctuation is still not negligible comparing to the relatively weak signal. In the meanwhile, the residual is also filter-parameter dependent. In this analysis, we focus on discussing the effect of the AP filter.

We add the simulated CMB temperature fluctuations to the signal map, which has resolution of 1.4 arcmin and the area of 2000 deg². The AP filter is applied with filter radius sizes varying between 2 arcmin, 1 arcmin and 0.8 arcmin. The results are shown in Fig. 7. As shown in the figure, the measured

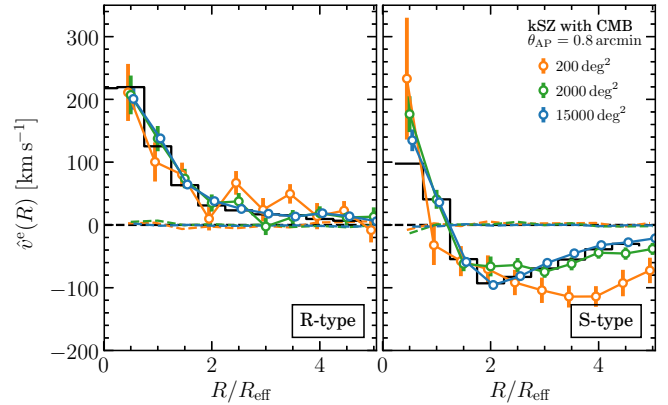
TABLE I: The summary of the significance and bias of the reconstructed radial velocity profile of voids with *Planck* data.

LSS Tracer					<i>Planck</i> maps					
SDSS Catalogue	N_{CG}	Effective Area	Void type	N_{void}	2D-ILC			SMICA-noSZ		
					χ^2_{NULL}	$\chi^2_{reduced}$	$\bar{\tau} \times 10^4$	χ^2_{NULL}	$\chi^2_{reduced}$	$\bar{\tau} \times 10^4$
DR12-LOWZ	386, 603	7, 943 deg ²	R-type	1, 462	7.11	0.33	1.24 ± 0.79	7.68	0.35	1.30 ± 0.77
			S-type	1, 348	8.78	0.98	-0.09 ± 0.41	7.71	0.85	-0.21 ± 0.38
DR12-CMASS	779, 070	8, 901 deg ²	R-type	3, 845	17.79	1.34	0.87 ± 0.46	14.69	1.34	0.59 ± 0.45
			S-type	3, 122	6.57	0.70	-0.12 ± 0.29	6.96	0.72	-0.17 ± 0.29
Combined	1, 165, 673	8, 901 deg ²	R-type	5, 307	21.86	1.19	1.03 ± 0.38	21.32	1.51	0.86 ± 0.38
			S-type	4, 470	6.10	0.62	-0.17 ± 0.24	4.86	0.45	-0.22 ± 0.24

FIG. 7: The simulated signal with added primary CMB as contaminations, assuming 2000 deg² survey area and $\theta_{FWHM} = 1.4$ arcmin resolution. The estimated $\hat{v}^e(R)$ with different AP filter radii are shown with different colors.

\hat{v}^e_R with 2 arcmin AP radius size (shown in orange color) has large errors. The errors are reduced with smaller AP filter radius size. With 2 arcmin, 1 arcmin and 0.8 arcmin AP size, we achieve 2.93σ , 7.68σ , 9.11σ detection for R-type voids; and 3.63σ , 11.82σ , 11.40σ for S-type. The corresponding fitted $\bar{\tau}$ are $(2.26 \pm 0.77, 2.95 \pm 0.38, 3.51 \pm 0.38) \times 10^{-4}$ for R-type voids ($\lambda_v < 10$) and $(2.88 \pm 0.79, 5.12 \pm 0.43, 4.66 \pm 0.41) \times 10^{-4}$ for S-type ($\lambda_v > 10$). The smaller value of $\bar{\tau}$ with larger AP radius size is due to the smear effect of the AP filter.

In the mean while, an obvious bias is shown at some scales, especially with large AP filter size. With different simulation realizations, we found that the amplitude and scales of the bias are varying. A possible reason of the bias is the residual structures of the CMB temperature fluctuation. The larger the AP filter size, the more residual CMB temperature fluctuation are existed in the estimation. On the other hand, the bias is also dependent on the number of samples. To investigate how the bias are varying with voids sample, we use different effective area of the simulated catalog, assuming CMB map resolution of 1.4 arcmin and AP filter size of 0.8 arcmin. The results are shown in Fig. 8. The green data in Fig. 8 shows the results assuming 2,000 deg² survey area, which includes 410 R-type and 174 S-type voids; The orange ones are the results by selecting only 10% of the survey area as the green ones, corresponding to reduce the survey area to 200 deg² and

FIG. 8: The simulated signal with CMB fluctuation residual as contaminations, assuming $\theta_{FWHM} = 1.4$ arcmin resolution and $\theta_{AP} = 0.8$ arcmin as filter radius. Different color indicate the results with different survey area.

including 36 R-type and 20 S-type voids; The blue data are the results with 15,000 deg², including 3,002 R-type and 1,403 S-type voids. With the survey area varied from 200 deg², 2,000 deg² to 15,000 deg², the $\chi^2_{reduced}$ vary from 1.81, 0.98 to 1.11 for the R-type voids, and from 3.94, 1.47 to 0.98 for the S-type voids. Given the d.o.f = 9, a $\chi^2_{reduced} = 1.00 \pm 0.47$ indicates a good fit.

B. Future experiments

The sensitivity and angular resolution of CMB experiments are being improved rapidly, with several on-going ground-based CMB observatories, such as SPT-3G [62], ACT [63], AdvACT [64–66], and Simons Observatory [67]. These ground-based CMB surveys will provide higher angular resolution CMB maps with lower noise levels in the near future. Here we plan to simulate the future detectability of ACT, AdvACT and Simons Observatory, by assuming that the angular resolution of these survey can reach $\theta_{FWHM} = 1.4$ arcmin. We assume that SPT-3G will cover 2,000 deg² survey area, AdvACT and Simons Observatory will cover 15,000 deg² area, respectively [67]. The latter one corresponds to the $f_{sky} \simeq 0.4$ but excluding Galactic plane. Beside the CMB temperature fluctuation, we further add instrumental noises

TABLE II: Forecasts for ACT, AdvACT and Simons Observatory detection of voids profile. The results with $\sigma_n = 0$ is the instrumental noise free case.

Survey Area [deg ²]	N_{CG}	σ_n [$\mu\text{K-arcmin}$]	Void type	N_{void}	χ^2_{NULL}	χ^2_{reduced}	$\bar{\tau} \times 10^4$	Experiments
2,000	50,250	0	R-type	410	147.91	0.98	3.51 ± 0.38	SPT-3G
			S-type	174	119.77	1.47	4.66 ± 0.41	
		10	R-type	410	45.46	0.94	4.30 ± 1.18	
			S-type	174	26.68	1.42	5.38 ± 1.27	
15,000	394,155	20	R-type	3002	26.79	0.84	3.03 ± 0.89	Pessimistic AdvACT
			S-type	1403	36.76	1.65	3.87 ± 0.82	
		10	R-type	3002	97.43	1.39	3.60 ± 0.51	Simons O./AdvACT
			S-type	1403	47.05	0.82	3.22 ± 0.46	
		6	R-type	3002	204.49	1.03	3.65 ± 0.34	Optimistic Simons O./AdvACT
			S-type	1403	133.48	1.89	3.68 ± 0.31	

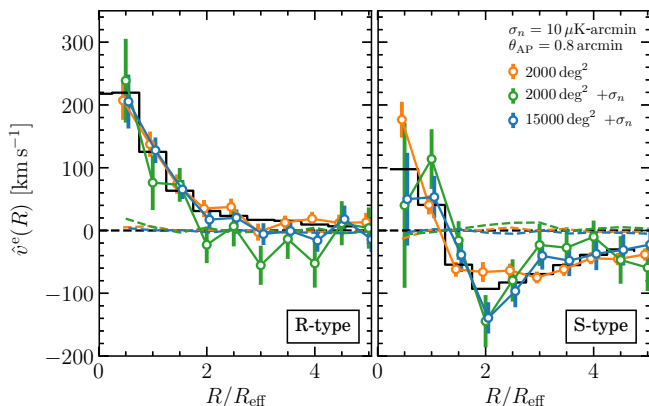


FIG. 9: The simulated signal with CMB fluctuation residual and thermal noise of $10\mu\text{K-arcmin}$, assuming $\theta_{\text{FWHM}} = 1.4$ arcmin resolution and $\theta_{\text{AP}} = 0.8$ arcmin AP filter radius. The result with $2,000\text{ deg}^2$ and $15,000\text{ deg}^2$ survey area are shown with different colors.

at different level according to different CMB experiments. We assume $10\mu\text{K-arcmin}$ *rms* noise for SPT-3G. For AdvACT, the *rms* noise level is around 10 to $20\mu\text{K-arcmin}$ so we assume that $\sigma_n = 20\mu\text{K-arcmin}$ as pessimistic case, and $\sigma_n = 10\mu\text{K-arcmin}$ as optimistic case. For Simons Observatory, we assume $\sigma_n = 10\mu\text{K-arcmin}$ as pessimistic case and $\sigma_n = 6\mu\text{K-arcmin}$ as optimistic case as indicated in Ref. [67]. The results are shown in Figs. 9 and 10; and the fitting values are summarized in Table II.

Figure 9 shows the results with *rms* = $10\mu\text{K-arcmin}$ noise added. The result with noise free is shown in orange color and the result with $2,000\text{ deg}^2$ survey area is shown in green. Although the estimated $\bar{\tau}$ is consistent with each other, the error is increased from $0.38(0.41) \times 10^{-4}$ to $1.18(1.27) \times 10^{-4}$ for R-type (S-type) voids. Even though the error is increased by a factor of 3, the further CMB experiments such as SPT-3G can still achieve $3.65\sigma(4.22\sigma)$ detection with $2,000\text{ deg}^2$ survey area.

If the survey area can be extended to $15,000\text{ deg}^2$, the estimation uncertainty can be reduced significantly. In the case of pessimistic case of AdvACT experiments, one can still achieve $3.4\sigma(4.73\sigma)$ detection for R-type (S-type) voids with noise

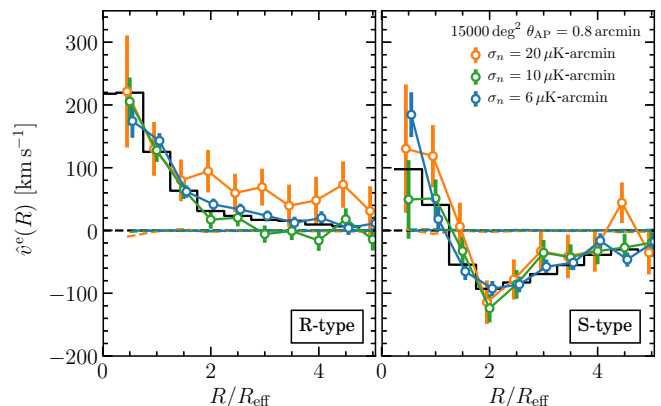


FIG. 10: The simulated signal with CMB fluctuation residual and thermal noise, assuming $\theta_{\text{FWHM}} = 1.4$ arcmin resolution and $\theta_{\text{AP}} = 0.8$ arcmin as filter radius. Different colors indicate the results with different thermal noise level.

rms = $20\mu\text{K-arcmin}$. With the optimistic AdvACT experiment or the pessimistic Simons Observatory, by assuming noise *rms* = $10\mu\text{K-arcmin}$, the detection can be improved to about 7σ for both R-type and S-type voids. With further optimistic case of noise *rms* = $6\mu\text{K-arcmin}$ for Simons Observatory, one can potentially achieve $\sim 10.7\sigma$ (R-type) and 11.8σ (S-type) detections with our estimator.

VI. CONCLUSION

In this paper, we develop an estimator to extract the mean radial velocity profile of the voids via the kinematic Sunyaev-Zeldovich effect of pairs of galaxies around the voids. We firstly test the estimator with the simulated pure kSZ maps, which are constructed from the BigMD *N*-body simulation [43, 44] and the void catalogue generated with the same simulation. The estimator is tested with the R-type and S-type voids separately and the results show that the mean radial velocity profile can be fully recovered with our estimator. With the simulated kSZ map, we note that the recovered signal is highly attenuated with the lower angular resolution of the map

or larger AP filter radius size, leading to the potential bias of optical depth.

We apply the estimator to the *Planck* 2D-ILC CMB map, with the LOWZ/CMASS galaxy and void catalogue. We conducted two statistics for the measured expansion profile of the void. One is the χ^2_{NULL} for NULL detection, which is calculated as the data against the zero line; the other is the χ^2_{reduced} which is calculated as the minimal χ^2 value between the data and the best-fitting theoretical profile. For the R-type and S-type voids, χ^2_{NULL} is calculated as 21.86 and 6.10 for the 2D-ILC map, which corresponds to the probability of 2.93×10^{-6} and 1.35×10^{-2} of null detection. This suggests that the R-type and S-type voids are measured at 3.31σ and 1.75σ C.L. respectively.

We also calculate the χ^2_{reduced} value as the minimal χ^2 of the data with respect to the theoretical expansion profile. For R-type voids, the $\chi^2_{\text{reduced}} = (0.33, 1.34, 1.19)$ with the DR12-LOWZ, DR12-CMASS and the combination of such two voids catalogue, respectively. We have 1.54σ measurement of the optical depth $\bar{\tau}$ with LOWZ catalogue, 1.94σ with CMASS catalogue and 2.68σ with the combination of such two catalogue. For the S-type voids, the measured $\bar{\tau}$ value is still consistent with 0.

We further investigate the effect of the CMB temperature fluctuation contamination, by adding simulated CMB map to the kSZ simulation map. The AP filter is applied to the simulated map. The results show that the CMB temperature fluctuation residual can increase the uncertainty of estimation and bias the results. The uncertainty and bias can be reduced with smaller angular size of AP filter and larger amount of voids

samples.

Finally, we forecast the detection for a few future CMB experiments with higher angular resolution and lower thermal noise. Beside the CMB contamination, we further add the instrumental noise at different level. The forecasts show that, experiment like SPT-3G can obtain $3.65\sigma(4.22\sigma)$ detection with $2,000 \text{ deg}^2$ survey area at $rms=10 \mu\text{K-arcmin}$; With $15,000 \text{ deg}^2$ survey area, experiment like AdvACT can obtain $3.4\sigma(4.73\sigma)$ detection for R-type (S-type) voids with noise $rms=20 \mu\text{K-arcmin}$; or about 7σ for both R-type and S-type voids at noise level of $rms=10 \mu\text{K-arcmin}$. Finally, in the case of $rms=6 \mu\text{K-arcmin}$, which is the most optimistic case of Simons Observatory, one can achieve over 10σ detection. Since the cosmic void is the most abundant structures of the large-scale Universe, our estimator opens a new window of probing dynamics of cosmic structures through the measurement of kinetic Sunyaev-Zeldovich effect.

Acknowledgments

We would like to thank Mathieu Remazeilles for supplying his *Planck* 2D-ILC map for this work and helpful discussion, and the useful discussion with Matthew Hilton and Anthony Walters. YZM would like to acknowledge the supports from National Research Foundation with grant no. 105925, 109577, 120378, and 120385, and National Science Foundation China with grant no. 11828301.

-
- [1] R. A. Sunyaev and Y. B. Zeldovich, *Comments on Astrophysics and Space Physics* **4**, 173 (1972).
- [2] R. A. Sunyaev and I. B. Zeldovich, *Monthly Notices of the Royal Astronomical Society* **190**, 413 (1980).
- [3] N. Hand, G. E. Addison, E. Aubourg, N. Battaglia, E. S. Battistelli, D. Bizyaev, J. R. Bond, H. Brewington, J. Brinkmann, B. R. Brown, et al., *Physical Review Letters* **109**, 041101 (2012), 1203.4219.
- [4] P. G. Ferreira, R. Juskiewicz, H. A. Feldman, M. Davis, and A. H. Jaffe, *Astrophysical Journal Letters* **515**, L1 (1999), astro-ph/9812456.
- [5] R. Juskiewicz, P. G. Ferreira, H. A. Feldman, A. H. Jaffe, and M. Davis, *Science* **287**, 109 (2000), astro-ph/0001041.
- [6] D. S. Swetz, P. A. R. Ade, M. Amiri, J. W. Appel, E. S. Battistelli, B. Burger, J. Chervenak, M. J. Devlin, S. R. Dicker, W. B. Dorise, et al., *The Astrophysical Journal Supplement Series* **194**, 41 (2011), 1007.0290.
- [7] C. P. Ahn, R. Alexandroff, C. Allende Prieto, S. F. Anderson, T. Anderton, B. H. Andrews, É. Aubourg, S. Bailey, E. Balbinot, R. Barnes, et al., *The Astrophysical Journal Supplement Series* **203**, 21 (2012), 1207.7137.
- [8] B. Soergel, S. Flender, K. T. Story, L. Bleem, T. Giannantonio, G. Efstathiou, E. Rykoff, B. A. Benson, T. Crawford, S. Dodelson, et al., *Monthly Notices of the Royal Astronomical Society* **461**, 3172 (2016), 1603.03904.
- [9] F. De Bernardis, S. Aiola, E. M. Vavagiakis, N. Battaglia, M. D. Niemack, J. Beall, D. T. Becker, J. R. Bond, E. Calabrese, H. Cho, et al., *Journal of Cosmology and Astroparticle Physics* **3**, 008 (2017), 1607.02139.
- [10] N. S. Sugiyama, T. Okumura, and D. N. Spergel, *Monthly Notices of the Royal Astronomical Society* **475**, 3764 (2018), 1705.07449.
- [11] Y.-C. Li, Y.-Z. Ma, M. Remazeilles, and K. Moodley, *Physical Review D* **97**, 023514 (2018), 1710.10876.
- [12] Planck Collaboration, P. A. R. Ade, N. Aghanim, M. Arnaud, M. Ashdown, E. Aubourg, J. Aumont, C. Baccigalupi, A. J. Banday, R. B. Barreiro, et al., *Astronomy and Astrophysics* **586**, A140 (2016), 1504.03339.
- [13] C. Hernández-Monteagudo, Y.-Z. Ma, F. S. Kitaura, W. Wang, R. Génova-Santos, J. Macías-Pérez, and D. Herranz, *Physical Review Letters* **115**, 191301 (2015), 1504.04011.
- [14] J. C. Hill, S. Ferraro, N. Battaglia, J. Liu, and D. N. Spergel, *Physical Review Letters* **117**, 051301 (2016), 1603.01608.
- [15] S. Ferraro, J. C. Hill, N. Battaglia, J. Liu, and D. N. Spergel, *Physical Review D* **94**, 123526 (2016), 1605.02722.
- [16] Planck Collaboration, N. Aghanim, Y. Akrami, M. Ashdown, J. Aumont, C. Baccigalupi, M. Ballardini, A. J. Banday, R. B. Barreiro, N. Bartolo, et al., *ArXiv e-prints* (2017), 1707.00132.
- [17] E. J. Baxter, B. D. Sherwin, and S. Raghunathan, *arXiv e-prints arXiv:1904.04199* (2019), 1904.04199.
- [18] R. K. Sheth and R. van de Weygaert, *Monthly Notices of the Royal Astronomical Society* **350**, 517 (2004), astro-ph/0311260.
- [19] M. C. Martino and R. K. Sheth, *arXiv e-prints* (2009), 0911.1829.

- [20] J. Clampitt, Y.-C. Cai, and B. Li, *Monthly Notices of the Royal Astronomical Society* **431**, 749 (2013), 1212.2216.
- [21] Y.-C. Cai, N. Padilla, and B. Li, *Monthly Notices of the Royal Astronomical Society* **451**, 1036 (2015), 1410.1510.
- [22] J. Dubinski, L. N. da Costa, D. S. Goldwirth, M. Lecar, and T. Piran, *The Astrophysical Journal* **410**, 458 (1993).
- [23] R. K. Sheth, H. J. Mo, and G. Tormen, *Monthly Notices of the Royal Astronomical Society* **323**, 1 (2001), astro-ph/9907024.
- [24] D. Tramonte, J. A. Rubiño-Martín, J. Betancort-Rijo, and C. Dalla Vecchia, *Monthly Notices of the Royal Astronomical Society* **467**, 3424 (2017), 1702.01788.
- [25] N. Hamaus, P. M. Sutter, and B. D. Wandelt, *Physical Review Letters* **112**, 251302 (2014), 1403.5499.
- [26] M. Cautun, Y.-C. Cai, and C. S. Frenk, *Monthly Notices of the Royal Astronomical Society* **457**, 2540 (2016), 1509.00010.
- [27] V. Demchenko, Y.-C. Cai, C. Heymans, and J. A. Peacock, *Monthly Notices of the Royal Astronomical Society* **463**, 512 (2016), 1605.05286.
- [28] E. Massara and R. K. Sheth, *arXiv e-prints arXiv:1811.03132* (2018), 1811.03132.
- [29] D. C. Pan, M. S. Vogeley, F. Hoyle, Y.-Y. Choi, and C. Park, *Monthly Notices of the Royal Astronomical Society* **421**, 926 (2012), 1103.4156.
- [30] P. M. Sutter, G. Lavaux, B. D. Wandelt, and D. H. Weinberg, *The Astrophysical Journal* **761**, 44 (2012), 1207.2524.
- [31] S. Nadathur and S. Hotchkiss, *Monthly Notices of the Royal Astronomical Society* **440**, 1248 (2014), 1310.2791.
- [32] Q. Mao, A. A. Berlind, R. J. Scherrer, M. C. Neyrinck, R. Scocimarro, J. L. Tinker, C. K. McBride, and D. P. Schneider, *The Astrophysical Journal* **835**, 160 (2017), 1602.06306.
- [33] L. Ceccarelli, D. Paz, M. Lares, N. Padilla, and D. G. Lambas, *Monthly Notices of the Royal Astronomical Society* **434**, 1435 (2013), 1306.5798.
- [34] S. Raghunathan, S. Nadathur, B. D. Sherwin, and N. Whitehorn, *arXiv e-prints arXiv:1911.08475* (2019), 1911.08475.
- [35] D. Paz, M. Lares, L. Ceccarelli, N. Padilla, and D. G. Lambas, *Monthly Notices of the Royal Astronomical Society* **436**, 3480 (2013), 1306.5799.
- [36] Y.-C. Cai, A. Taylor, J. A. Peacock, and N. Padilla, *Monthly Notices of the Royal Astronomical Society* **462**, 2465 (2016), 1603.05184.
- [37] A. Pisani, E. Massara, D. N. Spergel, D. Alonso, T. Baker, Y.-C. Cai, M. Cautun, C. Davies, V. Demchenko, O. Doré, et al., *arXiv e-prints arXiv:1903.05161* (2019), 1903.05161.
- [38] S. Nadathur, P. M. Carter, W. J. Percival, H. A. Winther, and J. E. Bautista, *Physical Review D* **100**, 023504 (2019), 1904.01030.
- [39] Y.-C. Cai, M. Neyrinck, Q. Mao, J. A. Peacock, I. Szapudi, and A. A. Berlind, *Monthly Notices of the Royal Astronomical Society* **466**, 3364 (2017), 1609.00301.
- [40] Planck Collaboration, P. A. R. Ade, N. Aghanim, M. Arnaud, M. Ashdown, J. Aumont, C. Baccigalupi, A. J. Banday, R. B. Barreiro, J. G. Bartlett, et al., *Astronomy and Astrophysics* **594**, A13 (2016), 1502.01589.
- [41] Y.-C. Cai, N. Padilla, and B. Li, *arXiv e-prints arXiv:1410.8355* (2014), 1410.8355.
- [42] S. Nadathur, S. Hotchkiss, and R. Crittenden, *Monthly Notices of the Royal Astronomical Society* **467**, 4067 (2017), 1610.08382.
- [43] A. Klypin, G. Yepes, S. Gottlöber, F. Prada, and S. Heß, *Monthly Notices of the Royal Astronomical Society* **457**, 4340 (2016), 1411.4001.
- [44] F. Prada, A. A. Klypin, A. J. Cuesta, J. E. Betancort-Rijo, and J. Primack, *Monthly Notices of the Royal Astronomical Society* **423**, 3018 (2012), 1104.5130.
- [45] V. Springel, *Monthly Notices of the Royal Astronomical Society* **364**, 1105 (2005), astro-ph/0505010.
- [46] A. V. Kravtsov, A. A. Klypin, and A. M. Khokhlov, *The Astrophysical Journal Supplement Series* **111**, 73 (1997), astro-ph/9701195.
- [47] S. Gottloeber and A. Klypin, *ArXiv e-prints* (2008), 0803.4343.
- [48] A. Klypin and J. Holtzman, *ArXiv Astrophysics e-prints* (1997), astro-ph/9712217.
- [49] K. Riebe, A. M. Partl, H. Enke, J. Forero-Romero, S. Gottlöber, A. Klypin, G. Lemson, F. Prada, J. R. Primack, M. Steinmetz, et al., *Astronomische Nachrichten* **334**, 691 (2013).
- [50] Z. Zheng, A. L. Coil, and I. Zehavi, *The Astrophysical Journal* **667**, 760 (2007), astro-ph/0703457.
- [51] M. C. Neyrinck, *Monthly Notices of the Royal Astronomical Society* **386**, 2101 (2008), 0712.3049.
- [52] S. Nadathur, *Monthly Notices of the Royal Astronomical Society* **461**, 358 (2016), 1602.04752.
- [53] E. Komatsu, K. M. Smith, J. Dunkley, C. L. Bennett, B. Gold, G. Hinshaw, N. Jarosik, D. Larson, M. R.olta, and L. Page, *The Astrophysical Journal Supplement Series* **192**, 18 (2011), 1001.4538.
- [54] M. Remazeilles, J. Delabrouille, and J.-F. Cardoso, *Monthly Notices of the Royal Astronomical Society* **410**, 2481 (2011), 1006.5599.
- [55] J. Delabrouille, J. F. Cardoso, M. Le Jeune, M. Betoule, G. Fay, and F. Guilloux, *Astronomy and Astrophysics* **493**, 835 (2009), 0807.0773.
- [56] S. Basak and J. Delabrouille, *Monthly Notices of the Royal Astronomical Society* **419**, 1163 (2012), 1106.5383.
- [57] Planck Collaboration, Y. Akrami, M. Ashdown, J. Aumont, C. Baccigalupi, M. Ballardini, A. J. Banday, R. B. Barreiro, N. Bartolo, S. Basak, et al., *arXiv e-prints arXiv:1807.06208* (2018), 1807.06208.
- [58] J.-F. Cardoso, M. Martin, J. Delabrouille, M. Betoule, and G. Patanchon, *arXiv e-prints arXiv:0803.1814* (2008), 0803.1814.
- [59] B. Reid, S. Ho, N. Padmanabhan, W. J. Percival, J. Tinker, R. Tojeiro, M. White, D. J. Eisenstein, C. Maraston, A. J. Ross, et al., *Monthly Notices of the Royal Astronomical Society* **455**, 1553 (2016), 1509.06529.
- [60] Planck Collaboration, P. A. R. Ade, N. Aghanim, M. Arnaud, M. Ashdown, E. Aubourg, J. Aumont, C. Baccigalupi, A. J. Banday, R. B. Barreiro, et al., *Astronomy and Astrophysics* **586**, A140 (2016), 1504.03339.
- [61] J. Hartlap, P. Simon, and P. Schneider, *Astronomy and Astrophysics* **464**, 399 (2007), astro-ph/0608064.
- [62] B. A. Benson, P. A. R. Ade, Z. Ahmed, S. W. Allen, K. Arnold, J. E. Austermann, A. N. Bender, L. E. Bleem, J. E. Carlstrom, C. L. Chang, et al., in *Millimeter, Submillimeter, and Far-Infrared Detectors and Instrumentation for Astronomy VII* (2014), vol. 9153 of *Society of Photo-Optical Instrumentation Engineers (SPIE) Conference Series*, p. 91531P, 1407.2973.
- [63] M. Hilton, M. Hasselfield, C. Sifón, N. Battaglia, S. Aiola, V. Bharadwaj, J. R. Bond, S. K. Choi, D. Crichton, R. Datta, et al., *The Astrophysical Journal Supplement Series* **235**, 20 (2018), 1709.05600.
- [64] B. A. Benson, P. A. R. Ade, Z. Ahmed, S. W. Allen, K. Arnold, J. E. Austermann, A. N. Bender, L. E. Bleem, J. E. Carlstrom, C. L. Chang, et al., in *Millimeter, Submillimeter, and Far-Infrared Detectors and Instrumentation for Astronomy VII* (2014), vol. 9153 of *Proceedings of the SPIE*, p. 91531P, 1407.2973.
- [65] A. Suzuki, P. Ade, Y. Akiba, C. Aleman, K. Arnold, C. Baccigalupi, B. Barch, D. Barron, A. Bender, D. Boettger, et al., *Jour-*

- nal of Low Temperature Physics **184**, 805 (2016), 1512.07299.
- [66] S. W. Henderson, R. Allison, J. Ausermann, T. Baidon, N. Battaglia, J. A. Beall, D. Becker, F. De Bernardis, J. R. Bond, E. Calabrese, et al., Journal of Low Temperature Physics **184**, 772 (2016), 1510.02809.
- [67] P. Ade, J. Aguirre, Z. Ahmed, S. Aiola, A. Ali, D. Alonso, M. A. Alvarez, K. Arnold, P. Ashton, J. Ausermann, et al., Journal of Cosmology and Astro-Particle Physics **2019**, 056 (2019), 1808.07445.